A Fully Integrated CMOS Fluorescence Biochip for DNA and RNA Testing

Arun Manickam, Rituraj Singh, Mark W. McDermott, *Life Member, IEEE*, Nicholas Wood, Sara Bolouki, Pejman Naraghi-Arani, Kirsten A. Johnson, Robert G. Kuimelis, Gary Schoolnik,
and Arjang Hassibi, *Senior Member, IEEE*

***Abstract*— Design and successful implementation of a fully integrated CMOS fluorescence biochip for deoxyribonucleic acid (DNA)/ribonucleic acid (RNA) testing in molecular diagnostics (MDx) is presented. The biochip includes a 32 × 32 array of continuous wave fluorescence detection biosensing elements. Each biosensing element is capable of having unique DNA probe sequences, wavelength-selective multi-dielectric emission filter (OD of 3.6), resistive heater for thermal cycling, and a high performance and programmable photodetector. The dimension of each biosensor is 100 μm × 100 μm with a 50 μm × 50 μm N_{well}-P_{sub} photodiode acting as the optical transducer, and a $\Sigma\Delta$ modulator-based photocurrent sensor. The measured photodetector performance shows ~116 dB detection dynamic range (10 fA–10 nA) over the 25 °C–100 °C temperature range, while being ~1 dB away from the fundamental shot-noise limit. To empirically demonstrate the compatibility of this biochip with MDx applications, we have successfully utilized the array and its thermal cycling capability to adopt a 7-plex panel for detection of six human upper respiratory viruses.**

***Index Terms*— Biochip, biosensor, fluorescence spectroscopy, image sensors, infectious disease, microarray, molecular diagnostics (MDx), nucleic acid, optical filter, polymerase chain reaction (PCR).**

I. INTRODUCTION

LEVERAGING the specificity of biomolecular interactions to detect the presence and abundance of biological analytes such as deoxyribonucleic acid (DNA), proteins, toxins, hormones, and other biomolecules is the underlying principle of biosensing [1]. Today, there are a multitude of biosensors categorized by their probe structure and transduction mechanism (e.g., optical [2]–[6], electronic [7], [8], or mechanical [9], [10]). Yet, the most widely used biosensors include DNA or antibody probes and adopt optical readouts, specifically continuous wave (CW) fluorescence transduction methods [4]–[6], [11], [12]. Such broad choice of probes is mainly due to the versatility of DNA and antibody probes and the available methods to biochemically synthesize or engineer them to recognize "almost" any target analyte biomolecule [13], [14]. The rationale behind using the CW fluorescence method is the availability of versatile fluorophore molecules as molecular tags (labels) [15] to identify and quantify biomolecules. Fluorescent labels, unlike their electrochemical, mechanical, or magnetic counterparts, are biocompatible, are easy to adopt in molecular biology, are easy to conjugate with probes and target analytes, have a high detection contrast (i.e., high signal-to-background in aqueous medium), have multiple colors, and are measurable using conventional microscopy instrumentation and scanners.

Here, we present an integrated CMOS biosensor array (biochip), designed and implemented specifically for CW fluorescence detection and nucleic acid [DNA or ribonucleic acid (RNA)] testing. In the past decade, there has been numerous reported CMOS biochips utilizing non-optical techniques such as electro-analytical [16]–[18] and magnetic [19], [20]. One can correctly claim that such non-optical biochips offer superior transducer compatibility for integration in standard CMOS. Nevertheless, such biosensors by and large require unconventional labels that offer no "color" and cannot be used in real-time detection assays that are common in molecular biology. Moreover, biocompatible surfaces (e.g., SiO_2 or Si_3N_4) are not always compatible with non-optical transducers. Examples are CMOS electro-analytical biosensors that require Faradaic electrodes built using Au or Pt [21], [22]. Hence, their adoption in applied fields such as molecular diagnostics (MDx), genomics, and proteomics research will be inferior to biochip platforms utilizing "gold standard" fluorescence techniques.

The focus of this paper is the system level design of the CMOS biochip and the implementation techniques to satisfy the stringent requirements of state-of-the-art DNA/RNA detection assays in MDx. In Section II, we first present the formulations and theoretical models of on-chip CW fluorescence-based detection. Next, we discuss the proposed system architecture which includes the integrated circuit components, the reaction chamber, surface chemistry, and the assay. In Section III, we discuss the circuit design implementation of the system in detail and report its measured performance, followed by Section IV, in which we explain the post-CMOS fabrication steps. In Section V, we report a successful implementation of an MDx panel

Manuscript received May 3, 2017; revised August 7, 2017; accepted September 5, 2017. Date of current version October 23, 2017. This work was supported by the National Human Genome Research Institute, National Institutes of Health, under Grant 5R44HG007626-03 and Award R44HG007626. This paper was approved by Guest Editor Peng Cong. *(Corresponding author: Arun Manickam.)*

The authors are with InSilixa, Sunnyvale, CA 94089 USA (e-mail: arun.manickam@insilixa.com).

Color versions of one or more of the figures in this paper are available online at http://ieeexplore.ieee.org.

Digital Object Identifier 10.1109/JSSC.2017.2754363

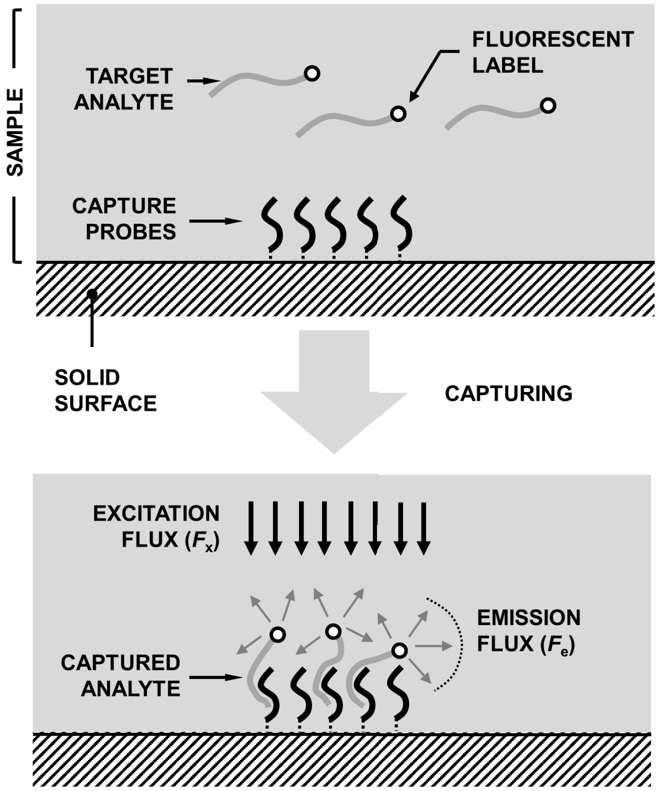

Fig. 1. Fluorescence biosensor with immobilized capture probes for analyte detection.

for upper respiratory viruses using a polymerase chain reaction (PCR [23])-based assay.

II. Specifications

A. CW Fluorescence Detectors

Fluorescence-based detection relies on excitation of electrons in the valence band of unique molecules (fluorophores [24]) by applying photon flux F_x at wavelength λ_x and detecting the return of the electrons to the ground state by monitoring the emitted photon flux F_e at wavelength λ_e ($\lambda_x < \lambda_e$). In fluorescence biosensors, depicted in Fig. 1, fluorophores are used as reporter molecules (labels) for the targets, while capturing probes are immobilized on a surface. The capturing of the targets by the probes results in aggregation of fluorophores on the surface which increases F_e at the probe coordinates.

To formulate this process, we use Beer–Lambert Law [25] which describes the transmitted photon flux, F_x^T(photons cm^{-2} sec^{-1}), through a medium with path length l (cm) that includes n absorbing fluorophore species in the sample with concentration C_n (M) as

$$F_x^T = F_x \cdot 10^{-\epsilon C_n l} \tag{1}$$

where ϵ (cm^{-1}M^{-1}) is the fluorophore absorption (extinction) coefficient at λ_x. Now in biosensors (Fig. 2), all the fluorophores are immobilized at the surface (i.e., $l \to 0$).

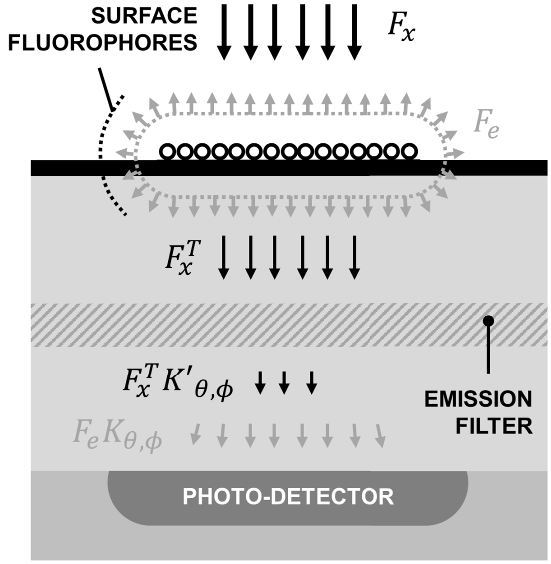

Fig. 2. Simplified cross section of a chip-based fluorescence biosensors system with an embedded photodetector beneath the capturing probe area.

Therefore, (1) becomes

$$F_x^T = \lim_{l\to 0} F_x \cdot 10^{-\epsilon\left(\frac{n\times 10^3}{N_A \cdot S \cdot l}\right)l} = F_x \cdot 10^{-\epsilon \frac{n_s}{N_A} 10^3} \tag{2}$$

where N_A, n_s, and S are the Avogadro's number, fluorophore surface concentration, and surface area, respectively. The photon absorption rate in this situation, denoted by A_x, is formulated by

$$A_x = F_x - F_x^T = F_x \left(1 - 10^{-\epsilon \frac{n_s}{N_A} 10^3}\right). \tag{3}$$

Now, assuming that $Q_Y(\lambda_e)$ is the quantum yield function of the fluorophore, described as the photon emission probability distribution function at λ_e, then the isotropic (in all directions) photon emission flux $F_e(\lambda_e)$ becomes

$$F_e(\lambda_e) = Q_Y(\lambda_e) A_x. \tag{4}$$

As depicted in Fig. 2, we can introduce parameter $K_{\theta,\phi}$ as the transmittance efficiency of $F_e(\lambda_e)$ originated from probe area S, to the photodetector. If the quantum efficiency of the photodetector is $Q_E(\lambda)$, then the emission-induced photocurrent I_{em} can be formulated by

$$I_{\text{em}} = q K_{\theta,\phi} S A_x \int_{\lambda=0}^{\infty} Q_Y(\lambda) Q_E(\lambda) d\lambda \tag{5}$$

where q is the charge of an electron. In practical systems, a fraction of F_x will always "leak" to the photodetector and create the background photocurrent I_{bk} such that

$$I_{\text{bk}} = q K'_{\theta,\phi} S F_x Q_E(\lambda_x) \tag{6}$$

where $K'_{\theta,\phi}$ is the transmittance efficiency of F_x^T. By combining (5) and (6), we can thus derive the signal-to-background ratio of the system as

$$\frac{I_{\text{em}}}{I_{\text{bk}}} = \left(\frac{K_{\theta,\phi}}{K'_{\theta,\phi}}\right)\left(1 - 10^{-\epsilon \frac{n_s}{N_A} 10^3}\right)\left(\frac{\int_{\upsilon=0}^{\infty} Q_Y(\upsilon) Q_E(\upsilon) d\upsilon}{Q_E(\lambda_x)}\right). \tag{7}$$

TABLE I

(A) NUMERICAL EXAMPLES OF SNR AND SIGNAL-TO-BACKGROUND RATIO OF A BIOSENSOR SYSTEM. (B) PARAMETERS

(a)

n_s	I_{em} (A)	$\frac{K_{\theta,\phi}}{K'_{\theta,\phi}}$	I_{bk} (A)	T (°C)	I_{dc} (A)	$\frac{I_{em}}{I_{bk}+I_{dc}}$	SNR_{max}
10^2	43f	10^2	1.9n	30	20f	2.29×10^{-5}	3.12
				90	5.5p	2.29×10^{-5}	3.11
		10^5	1.9p	30	20f	2.27×10^{-2}	3.02×10^3
				90	5.5p	5.89×10^{-3}	7.97×10^2
10^4	4.3p	10^2	1.9n	30	20f	2.29×10^{-3}	3.12×10^4
				90	5.5p	2.29×10^{-3}	3.11×10^4
		10^5	1.9p	30	20f	2.27	9.45×10^6
				90	5.5p	0.589	5.05×10^6

(b)

Parameter	Value	Parameter	Value
Photon flux density (F_x)	5×10^{17} cm^{-2} s^{-1}	**Max. quantum yield ($Q_Y(\lambda_e)$)^1**	0.04
Probe surface area (S)	2500 μm^2	**Transmittance efficiency ($K_{\theta,\phi}$)**	0.25
Diode surface area	2500 μm^2	**Max. photodiode Q_E^{2}**	0.38
Max. extinction coefficient (ϵ)^1	150,000 cm^{-1}M^{-1}	**Detection bandwidth (BW)**	1 Hz

[1] Values are for Cyanine-3 (Cy3) fluorophore [15].

[2] Typical value for N_{well}-P_{sub} diode in 0.25μm CMOS process.

The significance of (7) is that it demonstrates the independence of I_{em}/I_{bk} to F_x. Furthermore, it demonstrates that the optimal approach to achieve high I_{em}/I_{bk}, is to increase $K_{\theta,\phi}/K'_{\theta,\phi}$, the wavelength selectivity of the detector as the other parameters in (7) (e.g., ϵ or n_s) are constrained by the assay and the involved chemistry and not the detector.

Another important parameter to consider in our models is the signal-to-noise ratio (SNR). Providing a closed-form equation for SNR of a detector is involved; however, calculating its upper limit SNR_{max} generally referred to as the shot-noise limit, is straightforward. If we assume that the detector dark current is I_{dc}, then SNR_{max} for the detection bandwidth of BW becomes

$$SNR_{max} = \frac{I_{em}^2}{2q\,(I_{em} + I_{bk} + I_{dc})\,BW}. \tag{8}$$

In Table I, we have provided some numerical examples to better illustrate the design tradeoffs according to the formulations above. As expected from (7), the wavelength selectivity (e.g., having a sharp emission filter) has a first-order effect on the SNR. Yet, at elevated temperatures I_{dc} becomes significant. This indicates that photodetector is required to have a high detection dynamic range (DDR) to be able to measure I_{em} in presence of large $I_{bk} + I_{dc}$ values. It is also suitable to build a photodetector with an input-referred noise smaller than the shot-noise of the background with an R.M.S. value of $(2q(I_{bk} + I_{dc})BW)^{1/2}$.

B. DNA/RNA Testing

Generally speaking, DNA/RNA analytes and probes have little bearing on the optical design of fluorescence biosensors as they only show absorption at wavelengths <310 nm [26], which ensures their non-interference with fluorescence detection within the 450–800 nm "useful" range. However, there are key specifications with respect to DNA probe immobilization that the biochip should always meet to ensure compatibility with DNA/RNA testing assays in MDx. The first is having a SiO_2 surface in contact with the aqueous sample [27]. The second requirement is the thermal stability of probes in pH buffer solutions (e.g., phosphate-buffered saline or tris-buffered saline [28]). The probes need to be stable up to 95°C to enable DNA/RNA amplification assays such as PCR processes [23]. The third specification is related to maximum probe density for target accessibility. In the case of DNA microarrays the "optimal" distance is suggested to be 6–9 nm ($\sim$1.2–2.8$\times10^4$ μm^{-2}) [27].

The number of elements within a biosensor array is a function of the number of analytes that one needs to detect multiplied by the required redundancy. In our CMOS biochip system, we have chosen to implement an array with 1024 (32 × 32) elements which is aligned with applications in MDx rather than life science research [29], [30].

C. Proposed Architecture

In Fig. 3(a), we show the proposed and implemented biochip module, which includes a CMOS IC, integrated emission filter, DNA probes, and an optically transparent fluidic cap which not only confines the aqueous sample on top of the chip, but also facilitates its insertion and removal using an inlet port and an outlet port, respectively. The CMOS IC not only provides the high DDR photocurrent sensing, but also integrated heating and temperature sensing. The biochip and the fluidic cap are both assembled on a single PCB substrate with an edge I/O connector on its periphery to access the chip electronics.

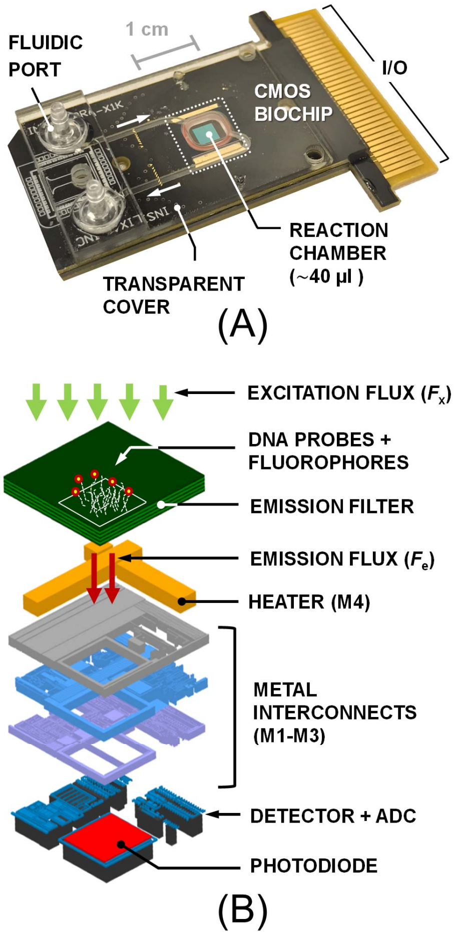

Fig. 3. (a) Implemented biochip module and (b) functional layers of an integrated CW fluorescence-based biosensor element (pixel).

TABLE II
BIOCHIP REQUIREMENTS

Parameter	Value	Justification
Biosensor dimensions	100µm × 100µm	Minimum practical pitch for probe spotting techniques
Number of biosensing elements	1024 (32 × 32)	Applicable to the broadest range of infectious disease applications and capable of running ~200 NAAT tests with sufficient redundancy
Detection dynamic range (DDR)	> 100 dB	Detecting I_D of 20fA – 10nA (Table IA)
Frame rate	~ 1Hz	Adequate for monitoring DNA hybridization kinetics (τ > 30s) with high OSR and DDR
Operating temperature	25°C – 100°C	Required for PCR (Fig.14)
Quantum efficiency ($Q_E(\lambda)$)	> 0.2 for 500nm $\leq \lambda \leq$ 600nm	Required for sufficient I_{em} values (Table IA)
Max. input photocurrent	10nA	Maximum $I_{\mathrm{bk}} + I_{\mathrm{dc}}$ (Table IA)
Photodetector noise contribution	< Input shot-noise	Fundamental noise limit for a current sensor (Section 3.2.1)
Temperature sensor resolution	< 0.5°C	Accuracy of PCR instruments ~ ±0.25°C [23]
On-chip heater power	10W	Required for achieving ramp rates for PCR > 5°C/s [23]
Optical filter rejection	> $10^{3.5}$ at λ = 490nm	Necessary for sufficiently high signal-to-background ratio ($\frac{I_{\mathrm{em}}}{I_{\mathrm{bk}}+I_{\mathrm{dc}}}$) (Table IA)
$K_{\theta,\phi}/K'_{\theta,\phi}$	> 1000	
Top surface material	SiO_2	Most suitable for conventional probe immobilization methods [27] (Section 2.2)
Surface probe density	~ 1.2 - 2.8 × 10^4 μm^{-2}	Optimal distance for target accessibility (Section 2.2)

In Fig. 3(b), we illustrate the functional layers of an integrated CW fluorescence-based biosensor element and in Table II we listed the key system requirements and their justifications. The DNA capture probes are immobilized on top of the filter (surface SiO_2). The fluorophores are located within the probe regions and are excited by an external LED-based photon flux that passes through the fluidic cap and the sample. Beneath the filter, we have the IC metal layers (four metal layers in our 0.25 μm CMOS process). The top metal (M4) includes a passive heater structure, while M1–M3 are used as interconnects as well as creating an optical aperture for an N_{well}-P_{sub}.

III. CIRCUIT IMPLEMENTATION

A. Photodetector Implementation

In our biochip, we implemented a first-order ΣΔ current-sensing modulator as the detector and a reverse-biased CMOS N_{well}-P_{sub} diode as the photon-to-electron transducer [31] within each biosensing element. The sensor input is the reverse-biased diode current, $I_D = I_{\mathrm{em}} + I_{\mathrm{bk}} + I_{\mathrm{dc}}$, which first feeds into a high dc gain integrator (Σ operator) followed by an analog-to-digital converter (ADC) (quantizer), as shown in Fig. 4(a). The digital output of the ADC which is the sensor output, also controls a digital-to-analog converter (DAC) to subtract an output-dependent current from the input (Δ operator).

There are multiple advantages of adopting this architecture in our system. First, it can achieve very high DDR (>100 dB [32]) compared to 3T or 4T architectures used CMOS image sensor [33], [34]. Second, it achieves superior noise performance due to ΣΔ operation [35]–[37]. Third, the architecture provides a digital output that can easily be read sequentially (scanned) in an array format. Finally, it can easily be integrated in the allocated 100μm × 100μm allocated silicon area. The disadvantages are the need for large oversampling ratios (OSR) and a fast oversampling clock to obtain the high DDR and the presence of idle-tones for very low input currents [38].

The high-level circuit diagram of the photodetector is shown in Fig. 4(b). The integrator is a capacitive transimpedance amplifier (CTIA) which integrates I_D on its feedback capacitor C_F while pinning the reverse-bias voltage of the photo-

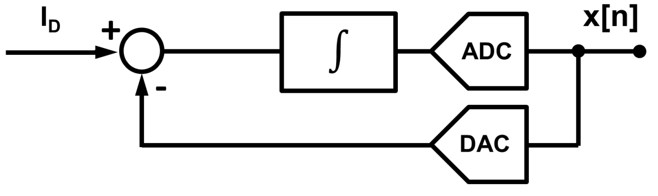

(A) BLOCK DIAGRAM

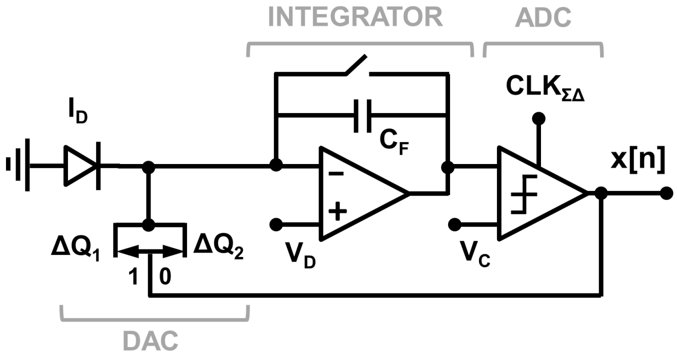

(B) CIRCUIT DIAGRAM

Fig. 4. (a) Photodetector block diagram and (b) its circuit diagram.

diode to V_D. The ADC is a clocked comparator, comparing the output of the CTIA with V_C, at every oversampling clock $\text{CLK}_{\Sigma\Delta}$ which has the frequency of $f_{\Sigma\Delta}$. The current DAC is implemented as a charge packet subtractor, which depending on the comparator output being 1 or 0, subtracts ΔQ_1 or ΔQ_2 from the CTIA input, respectively. It is important to note here that the $\Sigma\Delta$ modulator is insensitive to the offset at the V_C node as the offset is suppressed by its noise transfer function, given by (9), where f is the frequency [38]. In our system, we set $V_C = V_D$.

$$\text{NTF}(f) = 1 - e^{\left(-j2\pi \frac{f}{f_{\Sigma\Delta}}\right)}. \tag{9}$$

In Fig. 5, we show the detailed transistor and gate-level circuit implementation of the photodetector and its timing diagram. The core element of CTIA is a folded-cascode operational trans-conductance amplifier with an open-loop gain of ~80 dB and an output swing between 0.5–2 V. The capacitive feedback path of the integrator has the option to place C_{F1}(20 fF) or both C_{F1} and C_{F2}(180 fF) in the feedback loop by using the gain switch transistors M_{N10}-M_{N11}. A two-transistor switch structure M_{N7}-M_{N8} with a keeper switch M_{N9} is used for resetting and ensuring output-independent leakage current.

A Yukawa clocked comparator [39] is utilized for comparing V_{OUT}, output of the CTIA, with input V_c on the rising edge of $\text{CLK}_{\Sigma\Delta}$. Its output is then captured by an S-R latch, creating D_{OUT}, that can be read through column line $D_{\text{OUT}}[j]$ when ROW$[i]$ is selected.

The charge subtraction DAC path consists of a fixed current source, generating I_{REF}, and a pulse generator circuit applying I_{REF} periodically, in short pulses, to the CTIA input terminal. In this circuit, $\text{M}_{\Phi 1}$ and $\text{M}_{\Phi 2}$ serve as the current steering switches, i.e., when $\Phi_1 = 1$ and $\Phi_2 = 0$, the current is steered into the CTIA input, to perform the charge subtraction operation. When $\Phi_1 = 0$ and $\Phi_2 = 1$, the current sinks into V_D node. The pulse generation circuit first selects between CLK_1 and CLK_2 depending on whether D_{OUT} is 1 or 0, respectively, using gates I_1–I_4. The resulting output is then used to generate non-overlapping current steering signals, Φ_1 and Φ_2. The timing diagram of the system is shown in Fig. 5. Depending on CLK_1 and CLK_2, the applied pulse durations for current steering pulses are t_{p1} and t_{p2}, corresponding to subtracted charge of $\Delta Q_1 = t_{\text{p1}} I_{\text{REF}}$ and $\Delta Q_2 = t_{\text{p2}} I_{\text{REF}}$ from the charge stored in C_F.

As shown in Fig. 5, an analog bottom-plate sampling circuit has also been implemented for the test mode. This circuit samples V_{OUT} onto a sampling capacitor C_S (100 fF) which can then be read though the column analog output line $A_{\text{OUT}}[j]$, when ROW$[i]$ is selected. The analog sampling circuit is used for debugging and characterization in the test mode. In this mode, one can directly observe V_{OUT} to measure voltage and charge distribution offsets.

In Fig. 6(a) and (b), we show the layout and micrograph of the implemented photodetector. The total area is 100 μm ×100 μm with a photodiode fill-factor of 25%.

B. Photodetector Theoretical Performance

1) Saturation Level (Well Capacity): The maximum detectable input-current $I_{D_{\max}}$ occurs when the $\Sigma\Delta$ modulator feedback is continually subtracting, where

$$I_{D_{\max}} = \Delta Q_1 f_{\Sigma\Delta} = I_{\text{REF}} t_{\text{p1}} f_{\Sigma\Delta}. \tag{10}$$

Consequently, the "well capacity" Q_{well} for sampling period of $T_s = 1/BW$ and oversampling ratio, OSR $= f_{\Sigma\Delta} T_s$, becomes

$$Q_{\text{well}} = \frac{I_{\text{REF}} t_{\text{p1}} \text{OSR}}{q}. \tag{11}$$

In our design, I_{REF} is set to 1 μA, $f_{\Sigma\Delta} = 100$ kHz, and t_{p1} can be programmed to be 100 ns (low gain) or 10 ns (high gain), making $I_{D_{\max}}$ equal to 10 or 1 nA, respectively.

2) Noise Formulations: The main noise contributors in this photodetector are the photodiode and the current DAC. The total fluctuation in I_D can be formulated in the form of shot noise. The variance of the current fluctuations, σ_{D}^2 is computed by

$$\sigma_D^2 = 2q(I_{\text{em}} + I_{\text{bk}} + I_{\text{dc}})\text{BW}. \tag{12}$$

To derive the noise contribution of current DAC, we need to first consider the feedback current, $I_\Delta(t)$ as the multiplication of I_{REF}, and a current switching pulse train $p(t)$. Assuming that α_i's to be the fourier series coefficients of $p(t)$ and f_P being its fundamental frequency, it can shown that the $\overline{I_\Delta^2}(f)$, the power spectral density of $I_\Delta(t)$ is

$$\overline{I_\Delta^2(f)} = \sum_{k=0}^{\infty} \alpha_k^2 \overline{I_{\text{REF}}^2 (f - k f_P)} \tag{13}$$

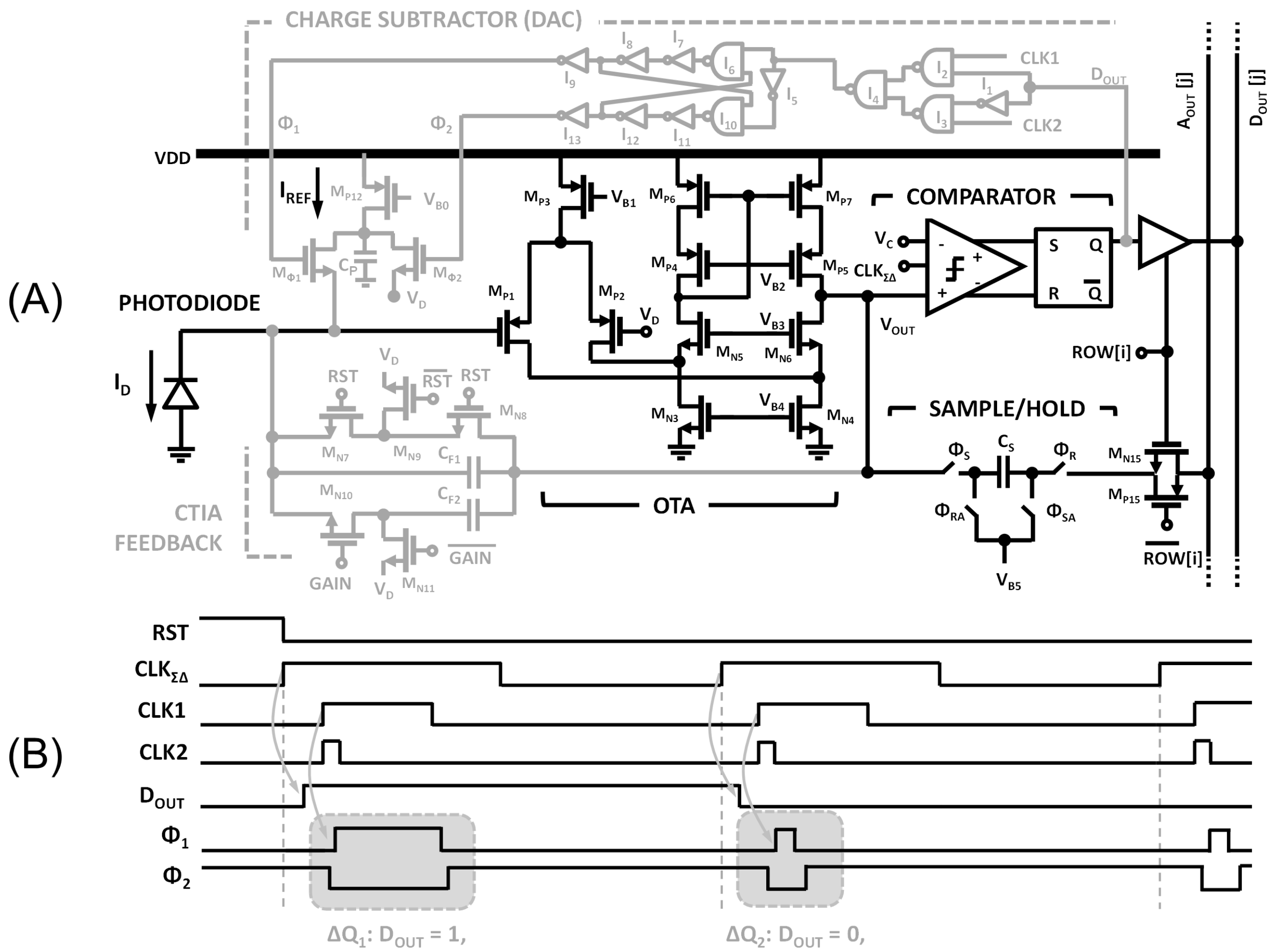

Fig. 5. (a) Detailed circuit schematic of the photodetector and (b) its timing diagram.

which can be used to formulate, σ_{Δ}^2 the variance of the noise contributed DAC, by

$$\sigma_{\Delta}^2 = \int_0^{\mathrm{BW}} \sum_{k=0}^{\infty} \alpha_k^2 \overline{I_{\mathrm{REF}}^2(f - k f_P)}\, df. \tag{14}$$

In our design, we considered the design criteria of $\sigma_{\mathrm{D}}^2 > \sigma_{\Delta}^2$ to ensure that the photodetector be shot-noise limited. The consequence of that, is that the transistor sizes become large in the current source to reduce the flicker-noise of I_{REF}.

C. Array Architecture

The top-level chip architecture of the biochip and the die photograph is shown in Fig. 7(a) and (b), respectively. The biochip has an array of 32 × 32 pixels including 13 temperature sensor pixels. These 13 temperature sensor pixels have the same circuitry as regular pixels, except that we cover the in-pixel photodiode with metal to block F_x^T, and use I_{dc} to measure the temperature. The temperature dependence of I_{dc} [40] is given by

$$I_{\mathrm{dc}} = I_0 e^{\left(-\frac{E_g}{xkT}\right)} \tag{15}$$

where I_0 is a constant, E_g is the bandgap energy, k is the Boltzmann's constant, x is a number between 1 and 2, and T is the absolute temperature.

Each element can individually be addressed through row and column decoders. The column multiplexer output $D_{\mathrm{OUT}}[i, j]$ signal is sent off-chip through low-voltage differential signaling buffer. The analog output chain makes use of analog column amplifiers, which are multiplexed at column level to generate the $A_{\mathrm{OUT}}\,[i, j]$ signal. All the clocks, row and column select signals, the analog reference voltages and power supply (3.3 V) are applied from off-chip.

The on-chip heating element is a 2.5 Ω passive multi-finger metal resistor, implemented using the top metal layer (M4) to deliver up to 10 W of power from a 5 V source. The resistive lines are evenly distributed out across the chip, passing through both the array and its periphery.

D. Off-Chip Components and Analysis

The reader electronics consists of a Spartan 6 XC6SLX16 field-programmable gate array (FPGA), DACs, ADCs, chip edge connector, and drivers for the LED electronics and heater modules (Fig. 8). The single bit output data-stream $D_{\mathrm{out}}[n, i, j]$, is fed into an array of sinc^2 filters in the FPGA for decimation and filtering. The FPGA then transfers the filtered data to the application software through a universal serial bus (USB) interface.

In the experimental setup, we create F_x using a low-power blue LED module (∼1 W of at 470 nm). The chip is mounted

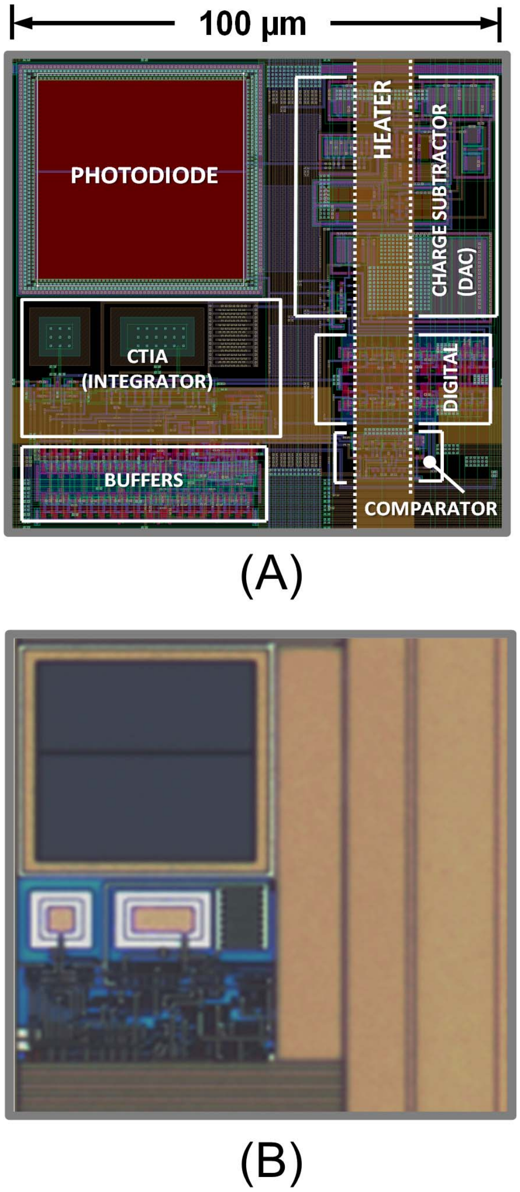

Fig. 6. (a) Biosensing element (pixel) layout and (b) its micrograph.

on an active heat sink consisting of a copper heat spreader and a fan. The active heatsink arrangement facilitates fast cooling of the chip when the on-chip heater is off. The temperature of the reaction chamber mounted on-chip is controlled using the on-chip heater, active heatsink, and the I_{dc} temperature sensors.

One practical challenge in measuring low levels of photocurrent is the ever presence of I_{dc}. To address this, we use correlated double sampling scheme, implemented off-chip using the FPGA and the application software. The LED module is periodically turned on and off and frames are collected from the chip during both ON ("bright" frame) and OFF ("dark" frame) phase. The dark frames are used to estimate I_{dc} and subtract it from I_D to obtain the $I_{\mathrm{em}} + I_{\mathrm{bk}}$. To remove the non-informative I_{bk} from the measurements, we then make use of array elements where no probe is immobilized and use the estimated I_{bk} to derive I_{em}. To reduce the error in estimation of I_{bk}, we average I_{bk} of several neighboring pixels to reduce the effect of spatial variation and additionally, perform a gain calibration at each pixel site, by recording the pixel values at different LED intensities.

TABLE III

CHIP PERFORMANCE SUMMARY

Parameter	Value
Technology	0.25µm CMOS
Supply voltage	2.5V
Die dimensions	7.0mm × 9.0mm
Array dimensions	32 × 32
Photodiode	50µm × 50µm (N_{well} - P_{sub})
Photodetector dark current (I_{dc})	20fA (30°C) – 5.5pA (90°C)
Photodetector $Q_E(\lambda)$	> 0.38 (500nm – 775nm)
Frame rate (BW)	1Hz – 50Hz
Well capacity (Q_{well})	6.25×10^{10} e^- (Low Gain) 6.25×10^{9} e^- (High Gain)
Maximum photocurrent ($I_{D\max}$)	10nA (Low Gain) at $f_{\Sigma\Delta}$ = 100kHz 1nA (High Gain) at $f_{\Sigma\Delta}$ = 100kHz
CLK_1, CLK_2 pulse width ($t_{\Phi 1,2}$)	10ns – 100ns
Detection linearity	> 10^5
Detection dynamic range (DDR)	116dB
Chip Output	102.4 Mbps LVDS serialized
Heating/cooling rate	4°C/s
Operating temperature range	25°C – 100°C
Temperature sensor resolution	0.3°C (for chip temperature 45°C – 100°C)
Total power consumption	62mW (array) + 50mW (LVDS) + 6mW (analog column amplifiers) = 118mW

E. Measurement Results

Fig. 9 shows the measured external quantum efficiency $Q_E(\lambda)$ of the photodiode. In Fig. 10, we report the mean I_{dc} measured across all pixels versus temperature. A calibrated thermocouple was placed very close to the chip surface utilizing thermal epoxy to record the die temperature. The error bars specify the minimum and maximum I_{dc} across the array measured at each temperature. Histograms of pixel dark current distribution at 30 °C and 90 °C are also shown in Fig. 10. As evident, at higher temperatures, "hot pixels" emerge at the outer edge of the array.

Fig. 11 shows the linearity performance of the photodetector, defined as $(I_D - I_{\mathrm{dc}})$ versus F_{x}. Different F_x values were generated by utilizing a combination of neutral density filters (10^1–10^6 attenuation) along with varying LED power settings. Measurements were taken using two different modes: 1) low-gain mode: $t_{\mathrm{p1}} = 100$ ns, $t_{\mathrm{p2}} = 0$ ($I_{D_{\max}} = 10$ nA); and 2) high-gain mode: $t_{\mathrm{p1}} = 10$ ns, $t_{\mathrm{p2}} = 0$ ($I_{D_{\max}} = 1$ nA). The OSR was set to 65535 with $f_{\Sigma\Delta} = 100$ kHz. As expected, we obtained very linear photodetection performance, over five orders of magnitude change ($\sim$10 fA–10 nA) in F_{x}.

Fig. 12 shows both the simulated and measured SNR versus F_{x}. The simulations adopt the formulations discussed in Section III-B to model the predicted SNR. Both the simulated and measured SNR drop from the shot-noise limit, near I_Q, defined as the input-current quantization limit, given by $I_Q \cong I_{D_{\max}}/\mathrm{OSR}$. Below this limit, not even a single transition should occur in $\Sigma\Delta$ modulator during the

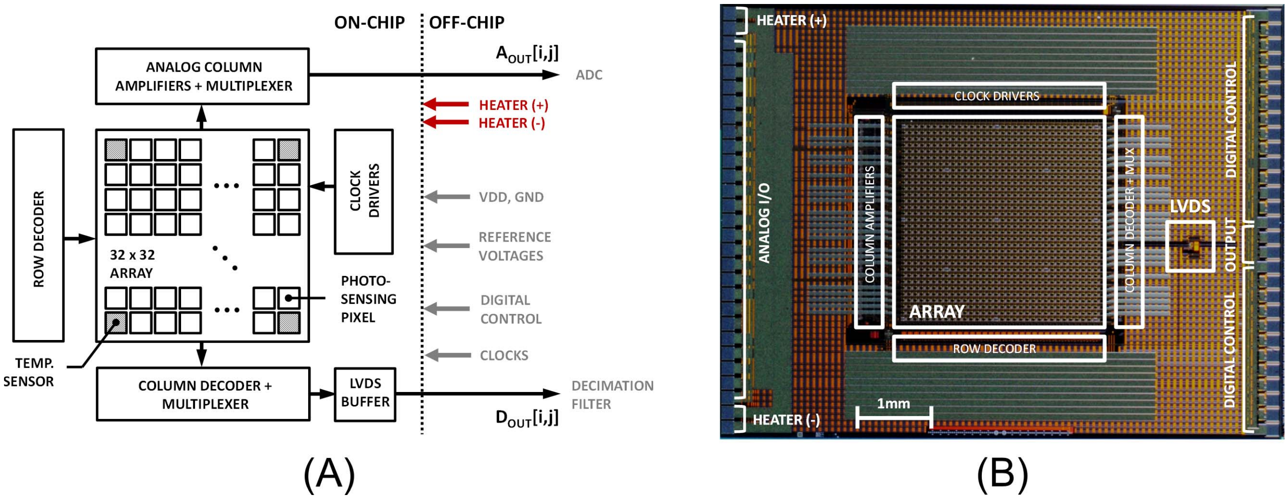

Fig. 7. (a) Chip architecture and (b) die micrograph.

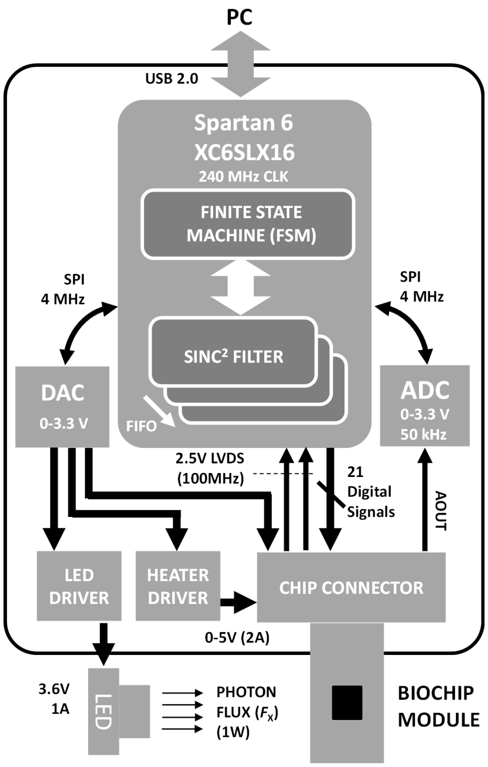

Fig. 8. CMOS biochip module reader architecture and functional components.

entire CLK$_{\Sigma\Delta}$ period. The lower limit of F_{x} occurs around 9×10^9 photons cm^{-2} s^{-1} and 9×10^{10} photons cm^{-2} s^{-1} corresponding to I_Q =15.2 and 152 fA for high-gain and low-gain modes, respectively. The SNR is close to its shot-noise limit at higher F_{x}, within ∼1 dB. Deviation from the limit at $F_{\mathrm{x}} > 10^{12}$ photons cm^{-2}s^{-1}, is believed to be due to additional fluctuation added by the LED excitation source and its driver electronics.

Table III summarizes the performance of the chip which matches the requirements that we set in Section II. Measurement techniques for CMOS image sensor characterization [41] were used to perform the aforementioned measurements.

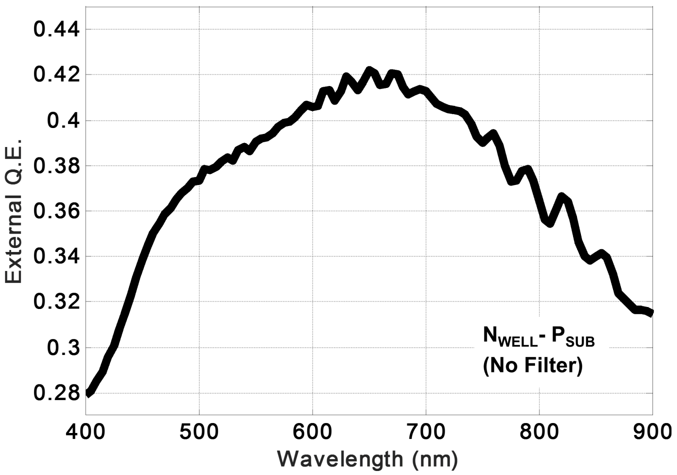

Fig. 9. Measured external quantum efficiency of the photodiode.

IV. POST-CMOS WAFER/CHIP PROCESSING STEPS

There are two key processing steps that need to be done after the CMOS wafers are manufactured, to convert the CMOS chip into a biochip. The first is the fabrication and patterning of the multi-dielectric emission filter and the second is the biofunctionalization of the surface.

A. Emission Filter

We utilize a long-pass multi-dielectric emission filter [42] to selectively reject F_x at λ_x and allow F_e to pass through. The filter is patterned and deposited on top of the CMOS wafer utilizing a lift-off process. The high and low index dielectric materials used for the filter are TiO_2 and SiO_2, respectively, with the exposed filter surface (top surface) being SiO_2. The filter coating is index matched to water at the peak of emission while the electric field at λ_x is maximized at the filter-water interface. The latter maximizes the surface-bound fluorophore excitation.

A disadvantage of interference filters is their high sensitivity to the angles of incidence (AOI). To address this challenge,

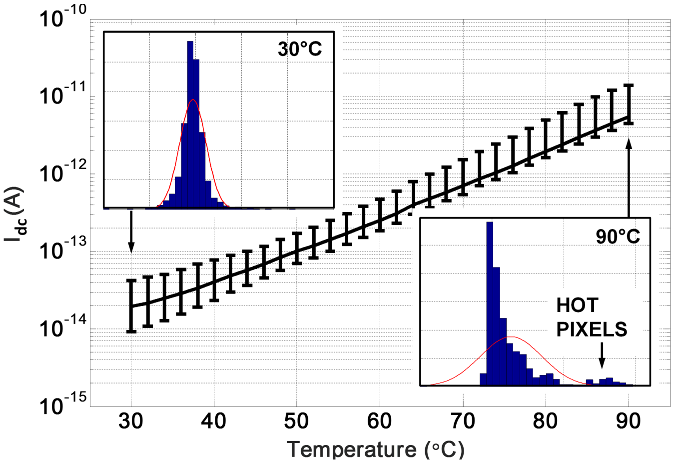

Fig. 10. Measured photodiode dark current (I_{dc}) versus temperature along with minimum and maximum spatial variations.

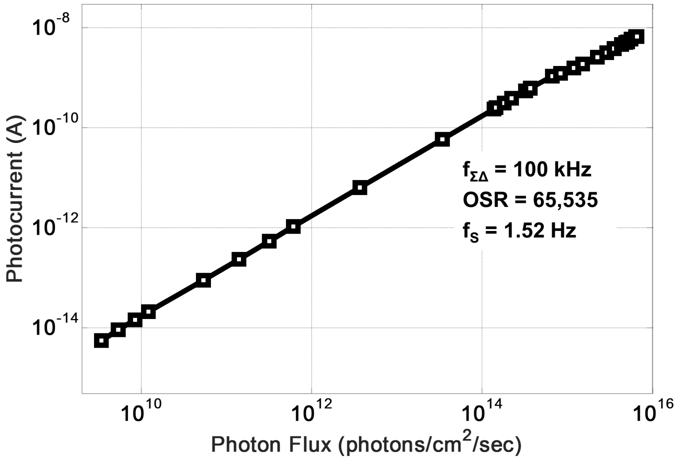

Fig. 11. Measured photodetector current vs. incident photon flux.

we utilize a two-pronged solution. First, we have optimized the layer thicknesses in the emission filter to minimize AOI sensitivity. For optimization, we have extensively used Essential McLeod Software (Thin Film Center, Tucson AZ) and chosen the solution-filter interface layer to maximize the E-field. Second, we created a dual fluorophore construct that offers 85 nm Stokes' shift, defined as the distance between peak emission and excitation.

Fig. 13(a) shows the cross-sectional scanning electron microscope (SEM) of the emission filter. The total filter thickness is ~8 μm. Fig. 13(b) shows the measured emission filter transmittance versus wavelength at different AOIs. The on-chip filter characterization is done using a light source with a monochromator. The wavelength is swept between 400 and 700 nm and the chip's response to different wavelengths is recorded. In Fig. 13(c), the measured excitation and emission spectrum of the fluorophore label is reported. The effective filter optical blocking ratio (OD) at λ_x = 490 nm (fluorophore peak excitation) is 3.6. For increasing AOIs up to 50°, the filter transmission band shifts only by 10 nm.

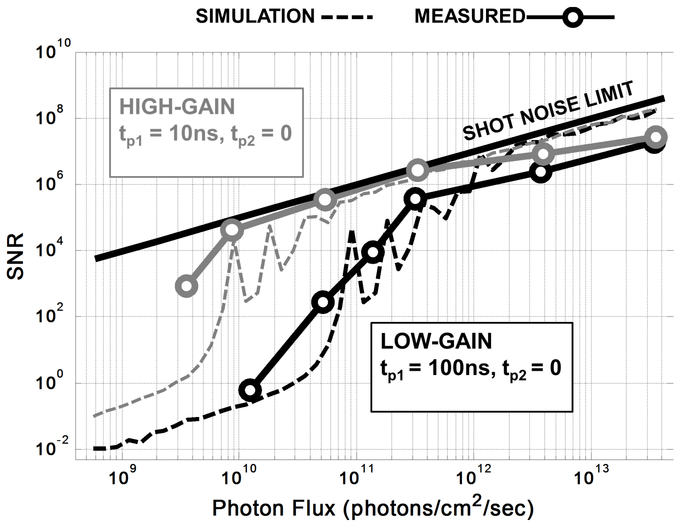

Fig. 12. Measured and simulated SNR versus photon flux for both high- and low-gain operating modes.

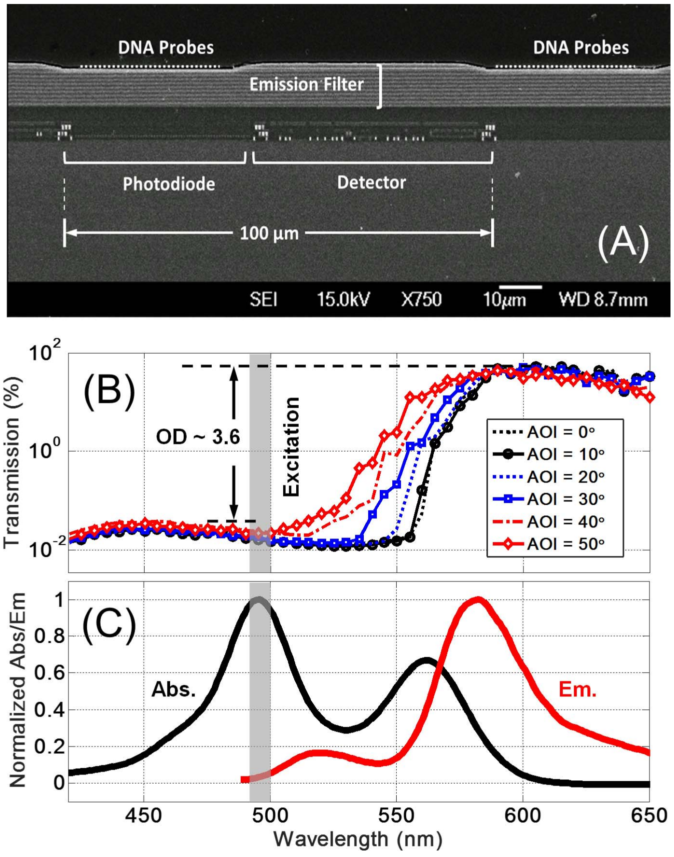

Fig. 13. (a) SEM cross section of the chip + integrated filter, (b) measured filter transmittance versus AOIs, and (c) excitation and emission spectrum of the dual fluorophore construct.

B. Surface Biofunctionalization

CMOS chips bonded to FR4 PCBs are first cleaned using oxygen plasma and subsequently are exposed to (3-glycidoxypropyl) trimethoxysilane in a chemical vapor deposition (CVD) system without breaking vacuum. At this point, the covalently linked thin film bears epoxy functional

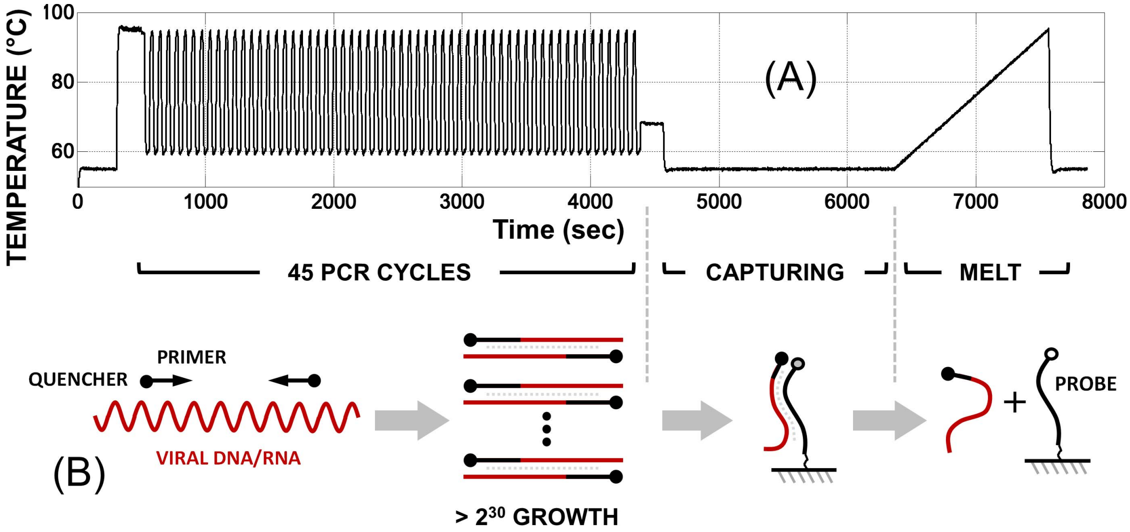

Fig. 14. (a) Temperature profile for NAAT workflow with PCR cycling, capturing (hybridization), and melt steps, and (b) conceptual molecular diagram describing these three steps.

TABLE IV

List of Pathogens Detected by NAAT Panel Along With the Probe Sequences Used for Solid-Phase Capturing and Melt

Pathogen Name	Probe Sequence (5'-3')
Influenza A (FluA)	Linker-GACCTAGTTGTTCTCGCCAGTGGAGGTCC-Fluor
Influenza B (FluB)	Linker-CACCGCAGTTTCAGCTGCTCGAATTGGGAGTTGAGGA- Fluor
Respiratory Syncytial Virus (RSV)	Linker-CTGTGTATGTGGAGCCTTCGTGAAGCTTCCATATTTGCC-Fluor
Human Parainfluenza Virus (HPIV)	Linker-GCGATTGATTCCATCACTTAGGTAAATTGGAAATGC- Fluor
Human Adenovirus C (AdvC2)	Linker-GCTCCACATAATCTAACACAAACTCCTCACCCCAGGTAAGATCGA- Fluor
Human Adenovirus E (AdvE)	Linker-TTTAATCATGGTTCTTCCTGTTCTTCCCTCCCAAATTGCA- Fluor
Polio (Positive Control)	Linker-TATCCGGTGAAAGTGAGATTCATTATCATTCGCTCCAT- Fluor
Negative Control	Linker-CAAAGTGGGAGACGTCGTTGT- Fluor

groups that can react chemo-selectively with terminally labeled primary amine functionalities of synthetic DNA probes [43]. Non-contact piezo printing is then used to deposit ∼80 pL droplets of DNA solution onto individual photodetector elements at 100 μm pitch. The printer's integrated real-time vision system and optical fiducial registration capabilities allow drop placement accuracy verification within ± 10 μm. Unreacted epoxy groups were rendered inert by treatment with a solution containing ethanolamine, a step that also removed excess (non-immobilized) DNA probes.

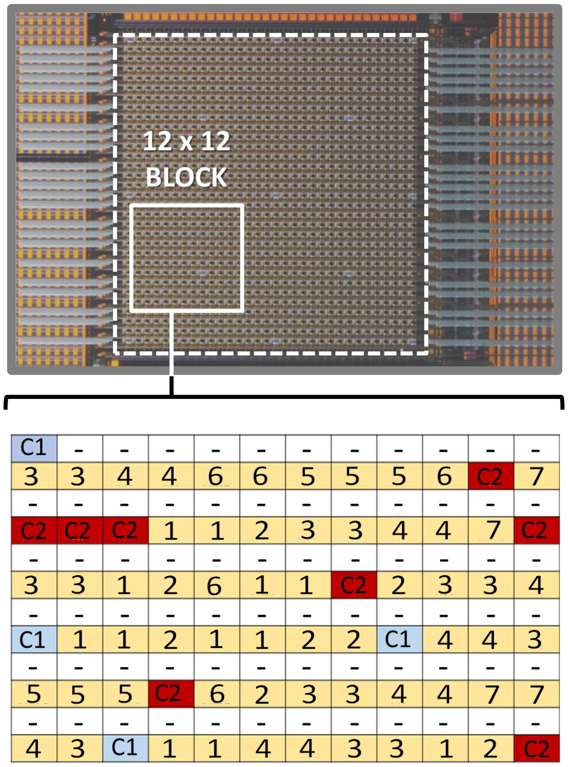

C1	-	-	-	-	-	-	-	-	-	-	-
3	3	4	4	6	6	5	5	5	6	C2	7
-	-	-	-	-	-	-	-	-	-	-	-
C2	C2	C2	1	1	2	3	3	4	4	7	C2
-	-	-	-	-	-	-	-	-	-	-	-
3	3	1	2	6	1	1	C2	2	3	3	4
-	-	-	-	-	-	-	-	-	-	-	-
C1	1	1	2	1	1	2	2	C1	4	4	3
-	-	-	-	-	-	-	-	-	-	-	-
5	5	5	C2	6	2	3	3	4	4	7	7
-	-	-	-	-	-	-	-	-	-	-	-
4	3	C1	1	1	4	4	3	3	1	2	C2

Fig. 15. Probe map for a 12 ×12 biosensing block. (1) FluA, (2) FluB, (3) RSV, (4) HPIV, (5) AdvC2, (6) AdvE, (7) Positive control and (8) Negative control. C1/C2 are quality control/calibration probes. White spots (-) are blank spots that can be used for I_{bk} subtraction.

V. Assay Implementation

To demonstrate the capabilities of our CMOS fluorescence biochip platform in detecting DNA/RNA from biological samples, we have successfully implemented a multi-analyte (multiplex) detection panel. This panel adopts a nucleic acid amplification testing (NAAT) method that includes PCR. The target analytes, to be detected by the chip, are seven common, unique respiratory pathogens listed in Table IV.

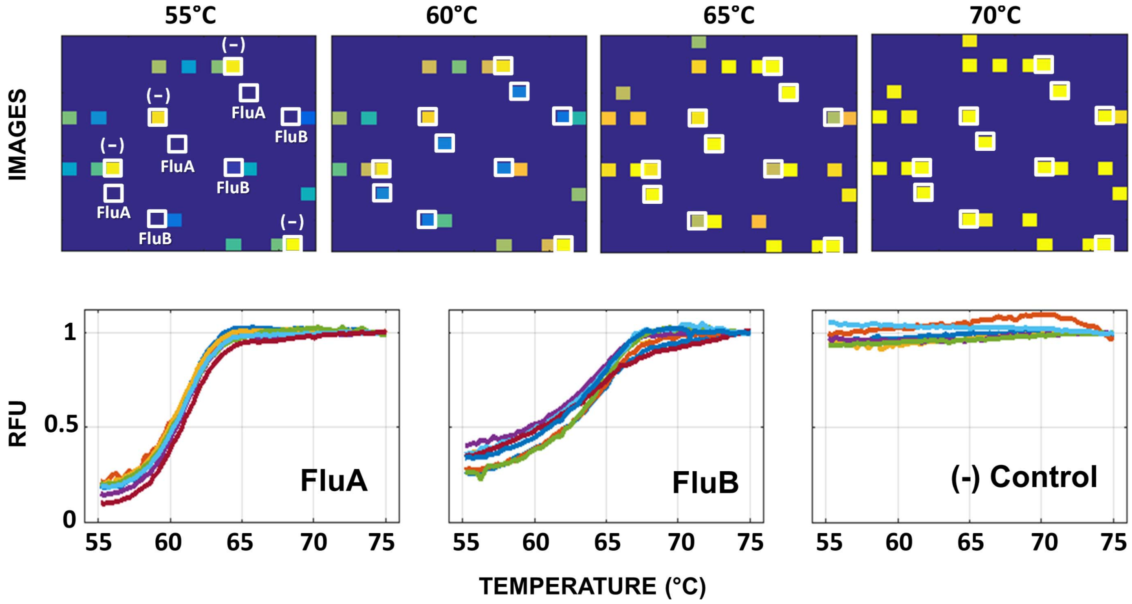

Fig. 16. Measured melt curves for a sample containing FluA and FluB. The top images shows array snapshots at four different temperatures. The bottom set of images show the melt curves obtained from individual spots containing probes for FluA, FluB, and negative control. The data is calibrated for temperature dependence of fluorophore intensity. It is expressed in relative fluorescence units.

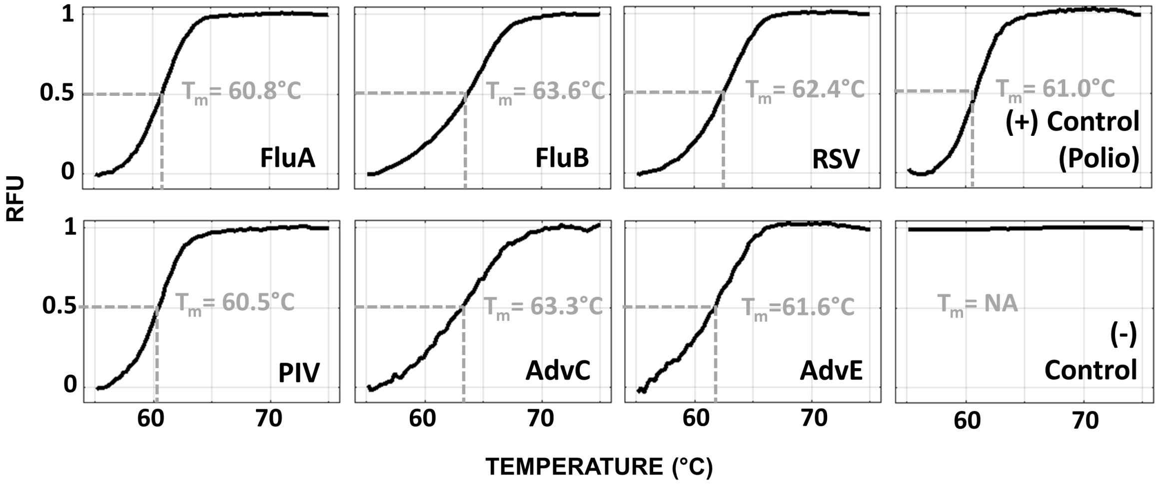

Fig. 17. Average melt curves from all the replicate spots for each of the seven pathogens and probes listed in Table IV. T_m refers to the melt temperature, i.e., the temperature at which 50% of hybridized probe-target complex has melted from the surface.

In Fig. 14(a), we show the chip workflow. In the first phase, during reverse transcription PCR enzymatic process [44], the sample goes through thermal cycling steps required to replicate (amplify) specific DNA/RNA sequence stretches (amplification factor $>2^{30}$) that are unique to individual pathogens in the sample. This is done by adding two short DNA sequences for each pathogen, generally referred to as primers, in the sample.

To enable the fluorescence detection of amplicons, we took advantage of an inverse fluorescence detection assay [45] [Fig. 14(b)]. In this approach, all the PCR primers are labeled with quencher molecules (BHQ2) for incorporation into generated amplicons. To detect these amplicons, we spot fluorescent labeled DNA capturing probes (see Table IV), targeting individual amplicons, at fixed coordinates of the array (probe map shown in Fig. 15). During the capturing step, the generated amplicons hybridize to the corresponding probes on the array, bringing the quencher in close proximity of fluorescent labels, and thereby temporarily reducing the fluorescence at the particular location. Therefore, by monitoring the signal reduction at different spots in the array, one can identify the target(s) present in the original sample. In addition to the target specific capture probes, there are positive and negative controls, quality control, and calibration probes present in the array, as shown in Fig. 15. The positive control provides an expected positive result due to the intentional addition of a known target nucleic acid to the reaction mix (Polio in our case). The negative controls work in the opposite manner, providing an expected negative result due to the absence of any corresponding target. Positive and negative controls help verify system functionality, determine repeatability and the level of non-specific signal in the system. Quality control probes are used to verify surface functionalization and DNA printing parameters. Calibration probes provide correction for fluorophore properties and any variation in LED illumination uniformity.

To improve the specificity of the signal, we also perform a high-resolution melt (HRM) analysis [46] of the hybridized target-probe complexes to confirm that the correct target is reducing the signal at the corresponding probe coordinates. HRM analysis makes use of the fact that each probe-target DNA complex has a unique dissociation curve as a function of temperature (also known as the "melt" curve). This dissociation curve is a function of different properties of the DNA complex such as guanine-cytosine content, length, sequence, and presence or absence of specific mutation and can serve as unique signature for a specific probe-target interaction. As shown in Fig. 14, the melt curve is performed by increasing the temperature from 55°C to 95°C and monitoring the return of the fluorescence signal as a function of temperature, as the probe-target complex "melts" and the target DNA is dissociated from the surface-bound complex.

In Fig. 16, we show the melt curve experimental results, including the array images and the relative fluorescence signal from different array elements for a sample containing FluA and FluB, as only the corresponding probes generate a melt curve signal and the negative control remained flat. In Fig. 17, we show averaged melt-curve results and the melting temperature T_{m} (defined as the temperature at which 50% of captured target-probe complexes detach from the surface), for all replicate spots, based on tests that include only one of the seven targets. The total time for experiment is ~2 hours, with ~1 hour of PCR cycling, ~0.5 hour of hybridization/capturing and ~0.5 hour of melt.

VI. CONCLUSION

In this paper, we demonstrate both in theory and practice that CW biosensors can be built using standard CMOS processes, without compromising any performance requirement that is critical for adoption in MDx or genomics research. As reported, CMOS ICs can be designed to include integrated photodetectors, thermal controllers, and all the essential electronic components; yet ICs do not offer any meaningful solution for the wavelength selectivity that CW fluorescence detection requires. As a result, we developed and integrated multi-dielectric interference filters to augment the photodetectors. The fabrication of these filters can easily be added to the CMOS process at a later stage.

When it comes to adopting "biology" on CMOS biochips, the focus should be on the surface and its biofunctionalization. In this paper, we show that conventional CVD techniques and non-contact printing methods can be utilized to create reliable and reproducible arrays of DNA probes. It is important to mention that at this point that these steps are not fully ready for high volume manufacturing. Therefore, their manufacturing cost is not comparable to the IC fabrication cost. However, with the reemergence of arrays in biotechnology and the current growth rate in MDx, we believe that this issue will be addressed by itself.

As a proof-of-principle, we reported the successful results of an NAAT panel in this paper. Clearly, the relatively small upper respiratory virus panel utilizes only a small fraction of the capabilities of our CMOS biochip. With 1024 biosensors in our chip, one can offer assays that can detect 100s of analytes simultaneously. This goal is exactly what we are aspiring to do in the next phase of this project.

ACKNOWLEDGMENT

The authors would like to thank R. Sinha for the bioinformatics design of primers and probe sequences, N. Gamini and P. Savalia for the biochip package design and assembly. Research reported in this publication was supported by the National Human Genome Research Institute of the National Institutes of Health under Award Number R44HG007626. The content is solely the responsibility of the authors and does not necessarily represent the official views of the National Institutes of Health.

REFERENCES

[1] F. G. Banica, *Chemical Sensors and Biosensors: Fundamentals and Applications*. Hoboken, NJ, USA: Wiley, 2012.

[2] H. Härmä, T. Soukka, S. Lönnberg, J. Paukkunen, P. Tarkkinen, and T. Lövgren, "Zeptomole detection sensitivity of prostate-specific antigen in a rapid microtitre plate assay using time-resolved fluorescence," *Luminescence*, vol. 15, no. 6, pp. 351–355, 2000.

[3] B. Liedberg, C. Nylander, and I. Lunström, "Surface plasmon resonance for gas detection and biosensing," *Sens. Actuators*, vol. 4, pp. 299–304, Jan. 1983.

[4] M. N. Kronick and W. A. Little, "A new immunoassay based on fluorescence excitation by internal reflection spectroscopy," *J. Immunol. methods*, vol. 8, no. 3, pp. 235–240, 1975.

[5] B. Jang, P. Cao, A. Chevalier, A. Ellington, and A. Hassibi, "A CMOS fluorescent-based biosensor microarray," in *IEEE Int. Solid-State Circuits Conf. (ISSCC) Dig. Tech. Papers*, Feb. 2009, pp. 436–437.

[6] D. E. Schwartz, E. Charbon, and K. L. Shepard, "A single-photon avalanche diode array for fluorescence lifetime imaging microscopy," *IEEE J. Solid-State Circuits*, vol. 43, no. 11, pp. 2546–2557, Nov. 2008.

[7] G. Davis, "Electrochemical techniques for the development of amperometric biosensors," *Biosensors*, vol. 1, no. 2, pp. 161–178, 1985.

[8] B. H. van der Schoot and P. Bergveld, "ISFET based enzyme sensors," *Biosensors*, vol. 3, no. 3, pp. 161–186, 1987.

[9] G. Wu, R. H. Datar, K. M. Hansen, T. Thundat, R. J. Cote, and A. Majumdar, "Bioassay of prostate-specific antigen (PSA) using microcantilevers," *Nature Biotechnol.*, vol. 19, no. 9, pp. 856–860, Aug. 2001.

[10] K. W. Wee *et al.*, "Novel electrical detection of label-free disease marker proteins using piezoresistive self-sensing micro-cantilevers," *Biosensors Bioelectron.*, vol. 20, no. 10, pp. 1932–1938, Apr. 2005.

[11] W. Trettnak and O. S. Wolfbeis, "Fully reversible fiber-optic glucose biosensor based on the intrinsic fluorescence of glucose oxidase," *Anal. Chim. Acta*, vol. 221, pp. 195–203, Dec. 1989.

[12] R. A. Bozym, R. B. Thompson, A. K. Stoddard, and C. A. Fierke, "Measuring picomolar intracellular exchangeable zinc in PC-12 cells using a ratiometric fluorescence biosensor," *ACS Chem. Biol.*, vol. 1, no. 2, pp. 103–111, 2006.

[13] J. Maynard and G. Georgiou, "Antibody engineering," *Annu. Rev. Biomed. Eng.*, vol. 2, no. 1, pp. 339–376, 2000.

[14] N. Hamaguchi, A. Ellington, and M. Stanton, "Aptamer beacons for the direct detection of proteins," *Anal. Biochem.*, vol. 294, no. 2, pp. 126–131, 2001.

[15] R. Y. Tsien and A. Waggoner, "Fluorophores for confocal microscopy," in *Handbook of Biological Confocal Microscopy*. New York, NY, USA: Springer, 1995, pp. 267–279.

[16] A. Manickam, A. Chevalier, M. McDermott, A. D. Ellington, and A. Hassibi, "A CMOS electrochemical impedance spectroscopy (EIS) biosensor array," *IEEE Trans. Biomed. Circuits Syst.*, vol. 4, no. 6, pp. 379–390, Dec. 2010.

[17] M. J. Milgrew, M. O. Riehle, and D. R. S. Cumming, "A 16×16 CMOS proton camera array for direct extracellular imaging of hydrogen-ion activity," in *IEEE Int. Solid-State Circuits Conf. (ISSCC) Dig. Tech. Papers*, Feb. 2008, pp. 590–638.

[18] C. Stagni *et al.*, "CMOS DNA sensor array with integrated A/D conversion based on label-free capacitance measurement," *IEEE J. Solid-State Circuits*, vol. 41, no. 12, pp. 2956–2964, Dec. 2006.

[19] H. Wang, Y. Chen, A. Hassibi, A. Scherer, and A. Hajimiri, "A frequency-shift CMOS magnetic biosensor array with single-bead sensitivity and no external magnet," in *IEEE Int. Solid-State Circuits Conf. (ISSCC) Dig. Tech. Papers*, Feb. 2009, pp. 438–439.

[20] D. A. Hall *et al.*, "GMR biosensor arrays: A system perspective," *Biosensors Bioelectron.*, vol. 25, pp. 2051–2057, May 2010.

[21] H. K. Seo, D. J. Park, and J. Y. Park, "Comparison of micro-and nano-pore platinum working electrodes for CMOS integrated nondisposable biosensor applications," *IEEE Sensors J.*, vol. 7, no. 6, pp. 945–946, Jun. 2007.

[22] P. M. Levine, P. Gong, R. Levicky, and K. L. Shepard, "Active CMOS sensor array for electrochemical biomolecular detection," *IEEE J. Solid-State Circuits*, vol. 43, no. 8, pp. 1859–1871, Aug. 2008.

[23] K. B. Mullis, F. Ferre, R. A. Gibbs, *The Polymerase Chain Reaction*. New York, NY, USA: Springer, 2012.

[24] J. R. Lakowicz, *Principles of Fluorescence Spectroscopy*, 3rd ed. New York, NY, USA: Springer, 2006.

[25] D. F. Swinehart, "The Beer-lambert law," *J. Chem. Edu.*, vol. 39, no. 7, p. 333, 1962.

[26] M. J. Cavaluzzi and P. N. Borer, "Revised UV extinction coefficients for nucleoside-5'-monophosphates and unpaired DNA and RNA," *Nucleic Acids Res.*, vol. 32, no. 1, p. e13, 2004.

[27] M. Schena, *DNA Microarrays: A Practical Approach*. New York, NY, USA: Oxford Univ. Press, 1999.

[28] R. Scorpio, *Fundamentals of Acids, Bases, Buffers and Their Application to Biochemical Systems*. Dubuque, IA, USA: Kendall Hunt, 2000.

[29] D. D. Dalma-Weiszhausz, J. Warrington, E. Y. Tanimoto, and C. G. Miyada, "The affymetrix GeneChip platform: An overview," *Methods Enzymol.*, vol. 410, no. 6, pp. 3–28, 2006.

[30] M. Schena, *Protein Microarrays*. Burlington, MA, USA: Jones & Bartlett Learning, 2005.

[31] H.-S. Wong, "Technology and device scaling considerations for CMOS imagers," *IEEE Trans. Electron Devices*, vol. 43, no. 12, pp. 2131–2142, Dec. 1996.

[32] R. Singh, B. Li, A. Elligton, and A. Hassibi, "A CMOS Σ-Δ photodetector array for bioluminescence-based DNA sequencing," in *Proc. Symp. VLSI Circuits (VLSIC)*, 2011, pp. 96–97.

[33] H. Eltoukhy, K. Salama, and A. E. Gamal, "A 0.18-μm CMOS bioluminescence detection lab-on-chip," *IEEE J. Solid-State Circuits*, vol. 41, no. 3, pp. 651–662, Mar. 2006.

[34] R. Singh, D. Ho, A. Nilchi, G. Gulak, P. Yau, and R. Genov, "A CMOS/thin-film fluorescence contact imaging microsystem for DNA analysis," *IEEE Trans. Circuits Syst. I, Reg. Papers*, vol. 57, no. 5, pp. 1029–1038, May 2010.

[35] W. Yang, "A wide-dynamic-range, low-power photosensor array," in *IEEE Int. Solid-State Circuits Conf. (ISSCC) Dig. Tech. Papers*, Feb. 1994, pp. 230–231.

[36] L. G. McIlrath, "A low-power low-noise ultrawide-dynamic-range CMOS imager with pixel-parallel A/D conversion," *IEEE J. Solid-State Circuits*, vol. 36, no. 5, pp. 846–853, May 2001.

[37] X. Wang, W. Wong, and R. Hornsey, "A high dynamic range CMOS image sensor with inpixel light-to-frequency conversion," *IEEE Trans. Electron Devices*, vol. 53, no. 12, pp. 2988–2992, Dec. 2006.

[38] R. Schreier and G. C. Temes, *Understanding Delta-Sigma Data Converters*. Hoboken, NJ, USA: Wiley, 2005.

[39] A. Yukawa, "A CMOS 8-bit high-speed A/D converter IC," *IEEE J. Solid-State Circuits*, vol. SSC-20, no. 3, pp. 775–779, Jun. 1985.

[40] S. M. Sze and K. N. Kwok, *Physics of Semiconductor Devices*. Hoboken, NJ, USA: Wiley, 2006.

[41] *EMVA Standard 1288-Standard for Characterization of Image Sensors and Cameras Release 3.0*, European Machine Vision Association, 2016. [Online]. Available: http://www.emva.org/wp-content/uploads/EMVA1288-3.0.pdf

[42] A. H. Macleod, *Thin-Film Optical Filters*. Boca Raton, FL, USA: CRC Press, 2001.

[43] F. Zhang *et al.*, "Chemical vapor deposition of three aminosilanes on silicon dioxide: Surface characterization, stability, effects of silane concentration, and cyanine dye adsorption," *Langmuir*, vol. 26, no. 18, pp. 14648–14654, 2010.

[44] L. Overbergh, D. Valckx, M. Waer, and C. Mathieu, "Quantification of murine cytokine mRNAs using real time quantitative reverse transcriptase PCR," *Cytokine*, vol. 11, no. 4, pp. 305–312, 1999.

[45] A. Hassibi, H. Vikalo, J. L. Riechmann, and B. Hassibi, "Real-time DNA microarray analysis," *Nucleic Acids Res.*, vol. 37, no. 20, p. e132, 2009.

[46] K. M. Ririe, R. P. Rasmussen, and C. T. Wittwer, "Product differentiation by analysis of DNA melting curves during the polymerase chain reaction," *Anal. Biochem.*, vol. 245, no. 2, pp. 154–160, 1997.

Arun Manickam received the B.E. degree in electronics and computer engineering from the College of Engineering, Guindy, Anna University, Chennai, India, in 2002, and the M.S.E. and Ph.D. degrees in electrical engineering from The University of Texas at Austin, Austin, TX, USA, in 2008 and 2012, respectively.

He has held engineering positions at Qualcomm, San Diego, CA, USA, Silicon Laboratories, Austin, and the Bosch Research and Technology Center, Palo Alto, CA, USA, in 2007, 2008, and 2010, respectively. He co-founded InSilixa, Inc., Sunnyvale, CA, USA, a CMOS biochip company, where he is currently an Engineering Manager. His current research interests include biosensors and bioelectronics, specifically the design and development of CMOS biochip platforms for medical diagnostic applications.

Rituraj Singh received the B.Tech. degree in electrical engineering from IIT Kanpur, Kanpur, India, in 2005, the M.A.Sc. degree in electrical and computer engineering from the University of Toronto, Toronto, ON, Canada, in 2009, and the Ph.D. degree in electrical and computer engineering from The University of Texas at Austin, Austin, TX, USA, in 2013.

He held engineering positions at Texas Instruments, Bengaluru, India, Mentor Graphics, Noida, India, and Silicon Laboratories, Austin, in 2004, from 2005 to 2006, and 2010, respectively. He was with InSilixa, Inc., Sunnyvale, CA, USA, from 2012 to 2017, where he was a member of the Co-Founding Team. His current research interests include circuits and systems for biological, medical, and consumer sensory applications.

Dr. Singh was a recipient of the Proficiency Medal for the Best B.Tech. Project in Electrical Engineering at IIT Kanpur in 2005 and the Distinguished Award Winner as part of Team InSilixa at the Nokia Sensing XChallenge Competition in 2013.

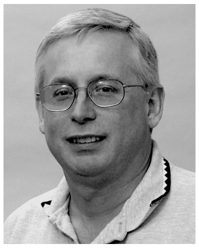

Mark W. McDermott (S'75–M'78–LM'14) was born in Detroit, MI, USA, in 1951. He received the B.S. degree in electrical engineering from the University of New Mexico, Albuquerque, NM, USA, in 1977, the M.S.E. and Ph.D. degrees in electrical engineering from the University of Texas, Austin, TX, USA, in 1988 and 2014, respectively.

He was a Senior Director with Apple, Inc., Cupertino, CA, USA, a VP/GM with Intrinsity, Inc., Austin, the VP of Engineering at Coherent Logix, West Lake Hills, TX, USA, the CEO of DynaFlow Computing, Inc., Austin, VP Engineering at Somerset Embedded Technologies, Inc., Austin, VP Engineering at VisionFlow, Inc., Austin, the GM and Director of the Texas Development Center for Intel Corporation, Austin, TX, USA, the Director of the PowerPC Somerset Design Center, Austin, and the Director of the Austin Design Center for Cyrix, Inc., Austin. He also co-founded DynaFlow Computing, The Learning Labs, Somerset Embedded Technologies, Inc., VisionFlow, Inc., Logical Silicon Solutions, Inc., Accelerated Solutions Corp., and MonoCom Systems, Inc. He is currently an Entrepreneur in Residence and Lecturer with the Electrical and Computer Engineering Department, University of Texas at Austin, where he teaches courses in silicon system design and technical entrepreneurship.

Dr. McDermott is a Registered Professional Engineer in the State of Texas and a member of ACM and TSPE. He holds 19 patents and 13 publications in the areas of VLSI design, engineering education and engineering management.

Nicholas Wood was born in San Antonio, Texas, in 1990. He received the B.S. degree in electrical engineering from the University of Texas, Austin, TX, USA, in 2013, and the M.S. degree in electrical engineering from the University of Texas at Dallas, Richardson, TX, USA, in 2016.

He is currently a Staff Engineer with InSilixa Inc., Sunnyvale, CA, USA, involved in embedded systems and software for CMOS biochips and biomedical instrumentation.

Sara Bolouki received the B.S. degree from the Amir Kabir University of Technology, Tehran, Iran, in 2000, the M.S. degree from Tehran University, Tehran, in 2002, and the M.S. degree from Stanford University, Stanford, CA, USA, all in electrical engineering.

She is currently a Senior Data Analyst with InSilixa, Inc., Sunnyvale, CA, USA. Her current research interests include statistics and machine learning.

Pejman Naraghi-Arani was born in Tehran, Iran, in 1969. He received the B.S. degree in biochemistry and the M.S. degree in chemistry from California State University, Fullerton, CA, USA, in 1991 and 1993, respectively, and the M.S. and Ph.D. degrees from the University of California, Davis, CA, USA, in 1996 and 2000, respectively, where he demonstrated the quasi-species nature of grapevine fanleaf nepovirus.

He completed post-doctoral training in the Enterovirus Branch at the Centers for Disease Control and Prevention, Atlanta, GA, USA, where he studied viral pathogenicity related to sequence variations. He spent almost 11 years as Group Leader, Molecular Assays, and Virology at Lawrence Livermore National Laboratory, Livermore, CA, USA, where he developed some 13 multiplex molecular assay panels in addition to work in biomarker discovery, predictive algorithms for viral evolution, and simplified sample preparation techniques. Since 2015, he has served as the Director of Research and Development, InSilixa, Inc, Sunnyvale, CA, USA.

Kirsten A. Johnson received the B.S. degree in genetics from the University of California, Davis, CA, USA, in 2004, and the Ph.D. degree in biological sciences from the University of California, Irvine, CA, USA, in 2012.

In 2002 and 2003, she was a Summer Intern at Lawrence Livermore National Laboratory, Livermore, CA, USA. From 2004 to 2006, she was a Biomedical Scientist at Lawrence Livermore National Laboratory, where she was involved in multiplex PCR assay development. She was a Post-Doctoral Fellow at the University of California, Irvine, CA, USA, from 2012 to 2013, focusing on host-pathogen interactions. She is currently a Senior Scientist with InSilixa, Sunnyvale, CA, USA, where she is involved in assay development.

Dr. Johnson is a member of the American Association for the Advancement of Science.

Robert G. Kuimelis was born in San Francisco, CA, USA, in 1966. He received the B.S. degree in chemistry from St. Mary's College, Moraga, CA, USA, in 1989, and the Ph.D. degree in organic chemistry from the University of California, Davis, CA, USA, in 1993.

He was a Post-Doctoral Fellow with Boston College, Chestnut Hill, MA, USA, from 1994 to 1996, focusing on non-natural nucleic acids and catalytic RNA mechanism. From 1996 to 1997, he was with Applied Biosystems, Foster City, CA, USA. From 1997 to 2002, he was with Phylos, Lexington, MA, USA. From 2002 to 2011, he was with Affymetrix, Santa Clara, CA, USA, as the Director of Chemistry. From 2012 to 2015, he was with HealthTell, Chandler, AZ, USA, as the Senior Director of Chemistry. Since 2015, he has been with InSilixa, Sunnyvale, CA, USA, as the Vice President of Chemistry. He has authored several book chapters and many published articles in the areas of nucleic acid chemistry and biophysics, surface chemistry and DNA/peptide/protein microarrays. He holds 27 issued United States Patents. His current research interests include interface of chemistry, biology and technology and the development of innovative platforms with broad potential to impact health.

Dr. Kuimelis is a member of the American Chemical Society.

Gary Schoolnik received the M.D. and clinical infectious diseases training from the University of Washington, Seattle, WA, USA, in 1972.

He was Intern, Junior, Senior, and Chief Resident in Medicine at the Massachusetts General Hospital, Boston, MA, USA, and was Research Associate and Senior Physician at the Rockefeller University in Manhattan. He is currently a Professor of Medicine, (Emeritus, Active) at Stanford Medical School, Stanford, CA, USA, and Attending Physician in Infectious Diseases and Internal Medicine at Stanford University Hospital, Stanford. He is also serving as the Chief Medical Officer with InSilixa, Sunnyvale, CA, USA. His current research interests include use of genomics, molecular biology and biochemistry to elucidate how bacteria cause disease and the use of this information to develop novel diagnostics and to identify drug targets, biomarkers and antigens.

Dr. Schoolnik serves or has served on a number of advisory boards including the National Advisory Allergy and Infectious Diseases Council, which is the principal advisory body of the National Institute of Allergy and Infectious Diseases.

Arjang Hassibi (S'99–M'05–SM'10) received the B.Sc. degree (Hons.) from the University of Tehran, Tehran, Iran, in 1997, and the M.Sc. and Ph.D. degrees in electrical engineering from Stanford University, Stanford, CA, USA, in 2001 and 2005, respectively.

He attended the post-doctoral training at the California Institute of Technology, Pasadena, CA, USA. He has held various research and development positions in both industry and academia, including second lieutenant at the Iranian Army Research Center, Tehran, from 1997 to 1999, the Stanford Microwave Integrated Circuits Laboratory, Stanford, from 1999 to 2005, the Stanford Genome Technology Center, Stanford, from 2001 to 2003, the CMOS High Speed Integrated Circuits Laboratory, California Institute of Technology, in 2005 and 2006, respectively, and Xagros Genomics, Sunnyvale, CA, USA, a startup company which he co-founded in 2001. He was a Faculty Member with the Electrical and Computer Engineering Department and the Institute for Cellular and Molecular Biology, The University of Texas at Austin, Austin, TX, USA, from 2006 to 2011, and a Visiting Professor with IBM Research at Yorktown, Yorktown Heights, NY, USA, in 2010 and 2011, respectively. Most recently, he was the Healthcare Thrust Lead with the Silicon Research Corporation. He has been the CEO and the Founder of InSilixa, Inc., Sunnyvale, since 2012. His current research interests include intersection of biotechnology and engineering, specifically biosensors and bioelectronics, biomedical electronics, and integrated sensors.